Optically pumped vector magnetometer using a strong bias magnetic field

Thomas Schönau,[1,*] Theo Scholtes,[1,†] Florian Wittkämper,[1] Alexander Sekels,[2] Stefan Hiebel,[2] Gregor Oelsner,[1] and Ronny Stolz[1]

[1] *Leibniz Institute of Photonic Technology, Albert-Einstein-Strasse 9, D-07745 Jena, Germany*
[2] *Sekels GmbH, Dieselstraße 6, D-61239 Ober-Mörlen, Germany*

(Received 19 August 2024; revised 6 November 2024; accepted 23 December 2024; published 4 February 2025)

We present an approach allowing an optically pumped magnetometer (OPM) to be operated within the Earth's magnetic field as a vector magnetometer, the sensitive axis of which can be freely defined. This approach enables the measurement of any vector component of the Earth's magnetic field with the same sensitivity. The OPM is realized by a microfabricated cesium-vapor cell with nitrogen buffer gas, which is immersed in a constant homogeneous bias field of approximately 730 μT. Since this bias field is about one order of magnitude stronger than the Earth's magnetic field, it defines the sensitive axis of the OPM. The bias field is generated by solid-state magnets and has been designed to exhibit a very low relative inhomogeneity ($< \pm 10^{-4}$ in relative units) within the vapor-cell dimensions as well as a point of vanishing temperature dependence at around 40°C. The OPM utilizes the light-narrowing effect, which enables effective suppression of spin-exchange relaxation even in such a large magnetic field amplitude. Based on this implementation, we demonstrate a white-noise floor of below 60 fT/$\sqrt{\text{Hz}}$ in the frequency interval between 100 Hz and 600 Hz and a 3-dB sensor bandwidth of > 5 kHz. Our approach enables unshielded ultrasensitive vectorial measurement capabilities that are relevant in many important applications.

DOI: 10.1103/PhysRevApplied.23.024006

I. INTRODUCTION

Ultrasensitive magnetic field detection plays a key role in many areas of research and industrial applications. It is used in, e.g., medicine for the detection of biomagnetic signals of the brain [1] and heart [2], nondestructive testing of material properties [3,4], and various geophysical and geotechnical applications. These include mineral and natural oil or gas exploration [5], unexploded-ordnance (UXO) detection [6,7], archaeology [8,9], and many other fields.

The choice of magnetometer type depends on the requirements specified by the respective application. In applications where sensitivity and bandwidth are considered the primary criteria and the associated use of cryogenics is not excluded, magnetometers based on superconducting quantum interference devices (SQUIDs) have long been considered the gold standard. For example, a white magnetic noise of 0.09 fT/$\sqrt{\text{Hz}}$ has been demonstrated by a SQUID magnetometer using a 29.5 mm × 33.5 mm sized pickup loop [10]. In recent decades, however, optically pumped magnetometers (OPMs) have made considerable progress and can now compete with SQUIDs in terms of noise performance. This offers the potential to replace SQUIDs by OPMs in various fields of application, as the latter do not require cryogenics and are thus easier to operate.

The improvements in sensitivity of alkali-based OPMs primarily involve the suppression of spin-exchange relaxation between alkali-metal atoms, which substantially reduces the transverse spin relaxation rate Γ_2 and consequently enhances the magnetic field sensitivity of OPMs [11]. The suppression of spin exchange can be achieved by two established modes of operation. The first is the spin-exchange relaxation-free (SERF) mode [11,12], which requires the SERF OPM to be operated in a near-zero magnetic field, typically of less than a few nanoteslas. Thus, SERF OPMs belong to the class of zero-field OPMs, which must be operated within a shielded environment or by applying active magnetic field compensation [13]. The best noise performance of a SERF OPM demonstrated has been 0.16 fT/$\sqrt{\text{Hz}}$ [14], using a measurement volume of 0.45 cm^3. An alternative way to suppress spin-exchange relaxation is through the light-narrowing (LN) regime, which requires pumping most of the alkali atoms into a stretched state [15], thus necessitating a high pump-laser power. The ability to operate in geomagnetic

*Contact author: thomas.schoenau@leibniz-ipht.de
†Contact author: theo.scholtes@leibniz-ipht.de

field strengths and above is the main advantage of LN OPMs, which are hence suited for geomagnetic applications without the need for magnetic field compensation techniques. The potential of the LN phenomenon becomes apparent when gradiometric setups [16–18] are considered, in which the technical noise can be strongly suppressed. In these cases, exceptionally low intrinsic noise can be demonstrated, which has even reached 0.54 $\mathrm{fT}/\sqrt{\mathrm{Hz}}$ [17]. In a more realistic scenario involving a portable magnetometer operated within a magnetic field of 50 μT, a sensitivity of 140 $\mathrm{fT}/\sqrt{\mathrm{Hz}}$ has been achieved, with technical noise representing the limiting factor [19]. A further class of highly sensitive OPMs is those using metastable ^{4}He instead of alkali vapor. Due to recent improvements in the laser and the sensor design, a zero-field OPM featuring a noise level of less than 50 $\mathrm{fT}/\sqrt{\mathrm{Hz}}$ has been demonstrated [20].

In the context of magnetic source detection and localization, vector magnetometers are preferred over scalar ones, because the solution space in inversion calculations and magnetic interpretations is reduced due to the additional information content and hence the numerical effort is much smaller compared to using scalar magnetometer data. Furthermore, in the relevant case of operation within the Earth's magnetic field, scalar magnetometers lack sensitivity to field fluctuations perpendicular to the magnetic field direction, as their sensitive axis is parallel to the Earth's magnetic field vector and is thus beyond the control of the operator. This fact is illustrated by decomposing a magnetic fluctuation $\Delta\vec{B} = \Delta\vec{B}_\parallel + \Delta\vec{B}_\perp$ into the components parallel and perpendicular to $\vec{B}$, respectively:

$$|\vec{B} + \Delta\vec{B}| \approx |\vec{B} + \Delta\vec{B}_\parallel| + \frac{|\vec{B}_\perp|^2}{2|\vec{B}|}. \tag{1}$$

For example, a variation of 1 nT perpendicular to the Earth's magnetic field (assuming 50 μT) results in a measurable change of only 10 fT for a scalar magnetometer. Thus, in typical scenarios in which the magnetic field fluctuations are significantly weaker than the Earth's magnetic field, scalar magnetometers effectively measure only the projection of these fluctuations onto the Earth's magnetic field vector. In order to be able to adequately replace vectorially measuring SQUIDs in geomagnetic applications such as transient electromagnetics (TEM) [21], OPMs require the Earth's magnetic field components to be measured along any spatial direction with a sensitivity significantly below 1 $\mathrm{pT}/\sqrt{\mathrm{Hz}}$, as otherwise fluxgate magnetometers could be used instead. At the same time, they must cover a bandwidth from dc to at least 1 kHz to also be suitable for electromagnetic methods in geophysics.

Several approaches have been documented in the literature that in principle enable vectorial measurements using OPMs operated in finite magnetic fields: One method to obtain full vector information involves monitoring several projections of the spin dynamics using probe lasers oriented in different directions [22–24]. Further approaches relate the magnetic field orientation to modulation amplitudes in the probe beam. These modulations are caused by: magnetically sensitive resonances in electromagnetically induced transparency (EIT) [25,26]; resonances in nonlinear magneto-optical rotation with frequency- or amplitude-modulated light [27,28]; free-alignment precession [29]; modulation of the magnetic field by coils [13,30–33]; parametric modulation of the longitudinal magnetic field [34]; modulation of the magnetic field by light shifts introduced by lasers from different directions [35]; and parametric resonances of ^{4}He metastable atoms in an actively compensated near-zero magnetic field [36].

All of the aforementioned approaches obtain the vector information from amplitude measurements, e.g., by measuring modulation amplitudes in the probe beam or by determining the coil current required for field compensation. However, amplitude measurements generally suffer from a limited signal-to-noise ratio (SNR) when compared to measurement of time or frequency. For example, to cover the measurement range of ±100 μT with a noise floor of 100 $\mathrm{fT}/\sqrt{\mathrm{Hz}}$, a normalized SNR of 180 $\mathrm{dB}/\sqrt{\mathrm{Hz}}$ is required. Using OPMs, only the work reported in Ref. [36] has come very close to this ambitious goal (175 $\mathrm{dB}/\sqrt{\mathrm{Hz}}$). Consequently, this is the only known work in which the required vectorial sensitivity has been achieved when operated within the Earth's magnetic field strength.

To circumvent the aforementioned limits related to amplitude measurements, we present a different approach in which each vector component is separately reduced to a high-precision frequency measurement [37]. This is achieved by exploiting the projection behavior described by Eq. (1). By exposing a conventional scalar LN OPM to a very homogeneous and temporally stable bias field, the field strength of which exceeds that of the Earth's magnetic field by at least one order of magnitude, it is basically sensitive only to the vector component parallel to the bias field. In other words, a single-axis vector magnetometer is obtained. Small systematic measurement errors arising from magnetic field variations perpendicular to the sensitive axis due to the quadratic terms in Eq. (1) can be corrected, if necessary, by employing a set of three such single-axis vector magnetometers arranged orthogonally to each other.

The paper is structured as follows. In Sec. II, we outline the influence of the nonlinear Zeeman effect in strong magnetic fields and present a compensation strategy allowing for high sensitivity of the magnetometer. The experimental setup is introduced in Sec. III and Sec. IV discusses the experimental results. In Sec. V, the results are summarized and a conclusion is drawn regarding the potential of this vectorial measurement approach.

II. OPM IN HIGH MAGNETIC FIELD

From the Breit-Rabi equation [38,39], an approximation for Zeeman transitions corresponding to $\Delta m_F = 1$ is obtained by a series expansion at $B = 0$ and neglecting the small contribution $g_I \mu_N \ll g_S \mu_B$:

$$E_{m_F+1} - E_{m_F} = \pm \frac{g_S \mu_B}{1+2I} B \mp \frac{g_S^2 \mu_B^2 (1+2m_F)}{(1+2I)^2 h \Delta\nu} B^2, \quad (2)$$

where $h\Delta\nu$ is the hyperfine splitting of the ground state, g_I is the nuclear g factor, I is the nuclear spin, and $F = I \pm \frac{1}{2}$ is the total angular momentum. For ^{133}Cs, $\Delta\nu \approx 9.19$ GHz, $g_I \approx 0.737$, and $I = 7/2$. The remaining parameters do not depend on the atom under consideration: the nuclear magneton $\mu_N \approx 5.05 \times 10^{-27}$ J/T, the electron g factor $g_S \approx 2$, and the Bohr magneton $\mu_B \approx 9.27 \times 10^{-24}$ J/T. As a consequence of Eq. (2), a critical field amplitude B_c can be introduced, above which the quadratic term becomes relevant. In magnetic fields $B < B_c$, the energy splitting of the Zeeman levels can be considered linear in B and independent of m_F, giving rise to a single transition frequency for all Zeeman coherences. In this case, the alkali atoms precess around the magnetic field vector $\vec{B}$ at the Larmor frequency,

$$f_L = \frac{g_S \mu_B}{(1+2I)h} |\vec{B}| = \frac{\gamma_L}{2\pi} |\vec{B}|, \quad (3)$$

where γ_L is the gyromagnetic ratio ($\gamma_L \approx 2\pi \times 3.5$ Hz/nT in the electronic ground state of ^{133}Cs). For magnetic field amplitudes $B > B_c$, the quadratic term in Eq. (2) becomes significant, leading to an approximately equidistant splitting of the transition frequencies proportional to m_F, which is known as the nonlinear Zeeman effect (NLZE). In ^{133}Cs, the splitting between two adjacent Zeeman transitions is

$$\Delta f_L \approx 2.67 \times 10^{-3} \frac{\text{Hz}}{\mu\text{T}^2} \times B^2. \quad (4)$$

If the frequency separation induced by this effect reaches or even exceeds the linewidth of the individual m_F transitions, it can be considered as an additional line-broadening or even splitting mechanism, which can considerably reduce the sensitivity of OPMs. The magnetic field strength at which this transition happens is a convenient definition of the critical magnetic field B_c. This reduction in sensitivity can occur even within the Earth's magnetic field when large-volume wall-coated vacuum cells with narrow magnetic resonance linewidths of $\lesssim 10$ Hz are used [28,40].

In the case of an OPM exposed to a strong bias field $B_0 > 500$ μT, the impact of the NLZE is even more relevant, thus requiring a compensation strategy. For illustrative purposes, the Mz magnetic resonance signal obtained during a preliminary study [41] of the NLZE in a strong magnetic field of 570 μT is shown in Fig. 1. The term Mz hereby indicates that the measured component of the atomic spins is parallel to the applied magnetic field. It clearly shows the equidistant splitting of approximately 870 Hz between adjacent Zeeman resonances according to Eq. (4).

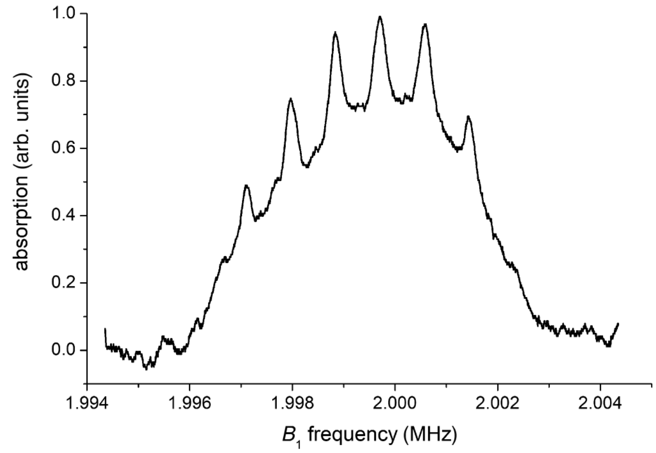

FIG. 1. The Mz magnetic resonance signal of a paraffin-coated Cs vacuum cell operated at room temperature, showing the nonlinear Zeeman effect at a strong magnetic field of approximately 570 μT. We have used a single laser beam for optical pumping and probing. The laser light has been tuned to the $F = 4 \rightarrow F' = 3$ Cs D_1 transition, circularly polarized, and had an optical power at the front of the cell of about 9 μW. The data have been taken from Ref. [41] for the purpose of illustration. In contrast, the work presented here employs the LSD-Mz operating mode to mitigate the adverse effects of the NLZE in conjunction with a microfabricated cesium-vapor cell containing nitrogen buffer gas at 180 mbar.

Known strategies to counteract the NLZE include the application of spin locking [42], increasing the overlap between Zeeman lines by using smaller-size buffer-gas cells to increase the linewidth [40], or using alkali metals in which the NLZE is less pronounced. We use ^{133}Cs, which exhibits a lower NLZE in comparison to ^{87}Rb or ^{39}K [38], and ensure sufficient overlap of Zeeman resonances by exploiting broadening mechanisms such as the use of microfabricated vapor cells, as well as focusing the magnetometer signal on a few Zeeman resonances by exploiting the LN effect in the light-shift-dispersed-Mz (LSD-Mz) configuration (see Refs. [43,44]).

An additional advantage of using relatively small-size vapor cells is the reduced requirements on the homogeneity of the bias field B_0. Furthermore, the use of buffer gas instead of a spin-preserving wall coating increases the linewidths of the Zeeman resonances and also pressure broadens the optical transitions. In the case of overlapping optical transitions, $F = \{3, 4\} \rightarrow F' = \{3, 4\}$, a single laser can be used to realize the LN effect [45]. This is achieved by tuning the laser wavelength such that the light couples strongly to the $F = 3$ ground state and only moderately pumps or probes the one with $F = 4$. As a consequence, the $F = 3$ manifold is strongly depleted and the population distribution is shifted toward the stretched states $|F, m_F\rangle = |4, -4\rangle$ or $|4, +4\rangle$, depending on the polarization of the pump beam (σ^- or σ^+, respectively). This shift toward the stretched states significantly suppresses the spin-exchange interaction and reduces the number of Zeeman resonances that contribute to the OPM signal, such that useful sensitivities can be achieved despite the smaller cell volume.

In the case considered here, the pump beam is aligned parallel to the bias magnetic field, which significantly increases the effectiveness of the optical pumping process. Further details on the LN effect and the LSD-Mz configuration are discussed in Sec. III and can also be found in Refs. [19,43,44,46].

Finally, by appropriately choosing the OPM operating point, it is possible to significantly broaden the Zeeman resonances with only a minor impact on the fundamental OPM sensitivity. This can be qualitatively explained by the fact that a simultaneous and matched increase in cell temperature and laser intensity enhances both the width and the amplitude of the measured magnetic resonance signal. The increase of the latter is partially compensating for the loss of sensitivity due to the increased linewidth. In this paper, this is referred to as "compensated broadening", in order to distinguish it from other broadening mechanisms, such as, e.g., due to magnetic field gradients. The compensated broadening mechanism of a temperature increase can be illustrated using the fundamental sensitivity of an OPM, which is limited by the spin-projection noise [47] (in units of $\mathrm{T}/\sqrt{\mathrm{Hz}}$):

$$B_{\mathrm{sp}} = \frac{1}{\gamma_L}\sqrt{\frac{\Gamma_2}{nV}}. \tag{5}$$

This fundamental sensitivity depends on the number of atoms nV in the measurement volume V and the transverse relaxation rate Γ_2 of the atoms, in units of hertz. The particle density of cesium at temperature T is given by

$$n = \frac{1}{T} \times 10^{27.866+A-B/T}\left[\frac{\mathrm{K}}{\mathrm{m}^3}\right], \tag{6}$$

with $A = 4.165$ and $B = 3830$ K [48]. The transverse relaxation rate Γ_2 is dependent upon several factors, including optical pumping and collisions of the alkali atoms with the cell wall or the buffer gas, as well as spin-exchange and spin-destruction interactions. The following is a worst-case analysis in which only the last two processes mentioned are taken into account, as these show the strongest increase with temperature:

$$\Gamma_2 \propto R_{\mathrm{SE}} + R_{\mathrm{SD}} = (\alpha + \beta) n \bar{v}. \tag{7}$$

The rates R_{SE} for spin exchange and R_{SD} for spin destruction are proportional to the particle density n as defined above and the average thermal velocity $\bar{v}$. The prefactors α and β take into account the different probabilities of the two relaxation processes. By substituting Eqs. (6) and (7) into Eq. (5), the dependency on the cesium density n is removed, yielding $B_{\mathrm{sp}} \propto \sqrt{\bar{v}} \propto T^{1/4}$. For instance, when the temperature is raised from 110°C to 120°C, the linewidth broadens by a factor of approximately 1.8, while the intrinsic noise limit only increases by 0.65%. In practice, the noise is typically dominated by technical factors, leading to deviating dependencies. However, this example clearly illustrates that the vapor temperature has a much greater influence on the linewidth than on the sensitivity. The possibility of increasing the linewidth by means of compensated broadening mechanisms has further advantages, as it reduces the requirements for the homogeneity of the strong bias field B_0 and increases the bandwidth of the OPM.

III. EXPERIMENTAL SETUP

A. LSD-Mz measurement principle

The measurement setup is sketched in Fig. 2, excluding the magnetic shielding barrel, the heater electronics, and the magnet system utilized for the generation of the bias magnetic field. The latter is implemented as a Halbach cylinder based on permanent magnets and will be described in detail in Sec. III C. The sensor head is mounted on a 10-mm-thick acrylic plate with outer dimensions of 130 mm × 80 mm. This plate is inserted into the Halbach cylinder such that the vapor cell is placed in the central region to ensure the best magnetic field homogeneity. Both the sensor head as well as the Halbach cylinder have been installed in a three-layer μ-metal magnetic shielding barrel of 1 m in diameter and 1 m length, described in detail in Ref. [49].

The laser light from a Toptica DLC DL Pro designed for the Cs D_1 transition at 894.6 nm is coupled into a polarization-maintaining single-mode optical fiber (F). At the sensor head, the light is collimated to a beam diameter of approximately 5 mm using a plano-convex lens (CL) prior to passing through a linear polarizer (LP). This conversion process is employed to address potential polarization variations that may arise from external factors such as vibrations or stress within the fiber, effectively transforming them into intensity variations. Subsequently, the horizontally and vertically polarized components of the light are split into two partial beams using a Wollaston prism (WoP). By rotation of the linear polarizer, the two sub-beams can be balanced for equal intensity.

Accordingly, the plane of polarization of the optical fiber is adjusted to maximize transmission through the linear polarizer as well. The two diverging sub-beams are parallelized by a pair of wedge prisms and reflected by a deflection prism (DP) in order to be aligned with the bias field $\vec{B}_0$. Since their polarization planes are orthogonal to each other, they can be converted into circular polarized beams with opposite helicity (σ^+,σ^-) by a properly adjusted quarter-wave plate (QWP).

The vapor cell is located in a thermally isolated chamber (C) at a temperature of typically 125°C. The chamber is equipped with two optical windows (OWs) and a coil in a Helmholtz-like configuration that generates the oscillating magnetic B_1 field in the y direction. After interaction with the Cs atoms, both beams will be reflected by a second deflection prism toward a pair of Hamamatsu S5106 photodiodes (PDs). It is worth noting that unlike commonly used balanced-detection methods, which determine the rotation of the plane of polarization of the light, this approach measures the absorption of the two partial beams. The photocurrents are converted to voltages using Femto DLPCA-200 low-noise transimpedance amplifiers (TIAs) and are recorded by a data-acquisition system (DAQ). The B_1 current is generated by a digital oscillator (OSC), the frequency of which can be controlled by the operator or, alternatively, by a proportional-integral-derivative (PID) controller.

In contrast to other OPM schemes [45,50,51], where the detected signal is oscillating at the Larmor frequency, only a quasi-dc signal that covers the bandwidth of the OPM of a few kilohertz needs to be acquired. This significantly reduces the demands on the electronics (TIAs, DAQ), especially in our case, where the Larmor frequency is around 2.6 MHz due to the 730 μT bias field. Furthermore, phase-sensitive (lock-in) detection is not required, eliminating the need for potentially costly equipment and avoiding systematic effects due to phase instabilities and shifts, as discussed in greater detail in Refs. [52,53]. A typical LSD-Mz magnetometer signal of our setup is depicted in Fig. 3. The spectra result from standard optically detected magnetic resonance (ODMR) principles and the partial beams are shifted relative to each other. One cause of this shift is the ac Stark effect, also known as light shift [54,55], which occurs due to off-resonant pumping. It can be interpreted as a fictitious magnetic field in the direction of the angular momentum of the light. Another cause of the observed shift is the NLZE discussed before. In the experimentally preferred case of equal intensities, resulting in exactly opposite fictitious magnetic fields as well as exactly opposite ($m_F \leftrightarrow -m_F$) Zeeman populations, the transmission spectra are shifted symmetrically in opposite directions. The LSD-Mz concept makes use of these shifts in order to obtain a dispersivelike signal by calculating the difference signal $I_{ph1} - I_{ph2}$ of the two beams, as indicated in Fig. 3. This difference signal exhibits a single steep slope that crosses zero at exactly the Larmor frequency, assuming that both beams are exactly balanced. The Larmor frequency can therefore be determined by operating the magnetometer in a feedback loop where a PID controller adjusts f_{B1} so that $I_{ph1} - I_{ph2} = 0$, resulting in $f_L(t) = f_{B1}(t)$. Since only the difference signal $I_{ph1} - I_{ph2}$ enters into the determination of the Larmor frequency, the magnetometer is expected to be inherently robust against technical noise, such as, e.g., light-intensity fluctuations. Also, systematic errors due to light shift or the NLZE that are also dependent on the pump rate, i.e., the light intensity, cancel each other out.

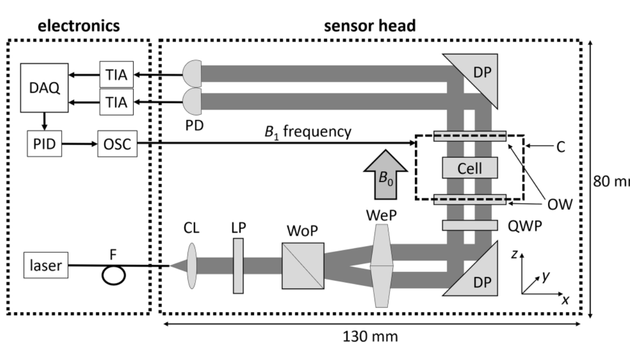

FIG. 2. The measurement setup. The details and a description of the abbreviations are given in the text.

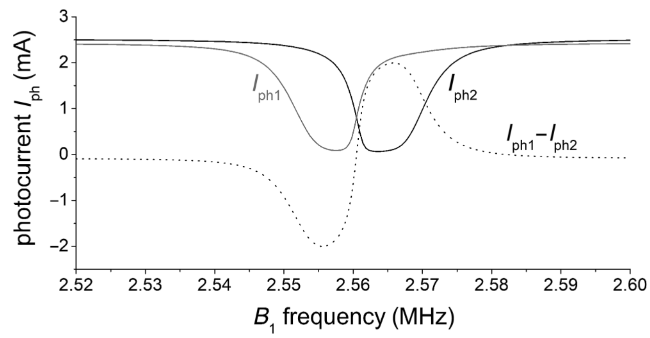

FIG. 3. The magnetic resonance signal of the two beams of an LSD-Mz OPM in a bias field of approximately 730 μT as well as the calculated difference signal. The operating point is the same as in Fig. 8.

B. Vapor cell

The central element of the OPM sensor head is the in-house microfabricated vapor cell shown in Fig. 4. The cavity of this cell is specifically designed for the LSD-Mz mode to be traversed by two adjacent parallel beams. A detailed description of the required cell-fabrication steps can be found in Ref. [56]. Nitrogen with a pressure of 180 mbar is employed as a buffer gas, fulfilling several crucial functions. These include reducing the collision rate

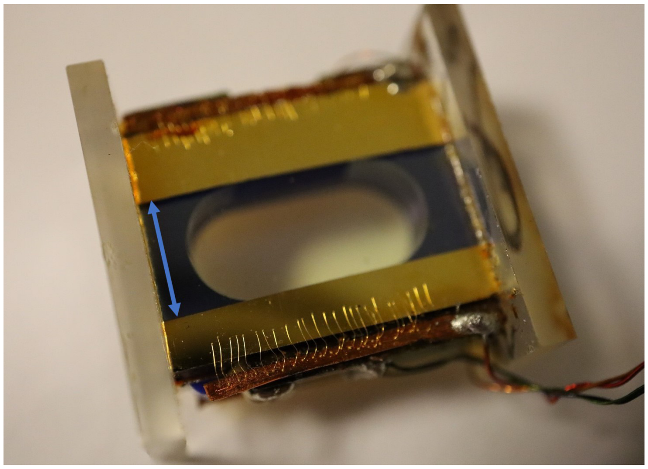

FIG. 4. A photograph of the vapor cell used in our experiments. The indicated dimension is 6 mm. See the text for details.

of the alkali metal with the cell walls, quenching [57], and broadening the absorption profiles of the optical transitions. A pump-beam diameter of approximately 5 mm has been chosen, resulting in a measurement volume of 157 mm^3 regarding both beams. The critical volume, in which the homogeneity of the bias field B_0 is crucial, is defined as $|x| \leq 5.5$ mm, $|y| \leq 2.5$ mm, and $|z| \leq 2$ mm, relative to the center of the vapor cell for a beam separation of 1 mm. For the definition of the coordinates, see Figs. 2 and 5.

Heating resistors, formed by a transparent resistive layer of indium tin oxide (ITO), are implemented directly on the outside of the optical windows to avoid the recondensation of Cs atoms on them, which could lead to unwanted beam scattering and potentially destroy the balance of the beams. The dimensions of the ITO layer are approximately 16 mm $\times$ 6 mm, with a thickness of 138 nm, resulting in a resistance of approximately 25 Ω for each window. The temperature of the vapor cell is monitored by a PT100 temperature sensor, which is glued to the silicon side wall, ensuring a good thermal contact.

The alternating current used to heat the ITO layers could potentially interfere with the Larmor precession of the Cs atoms, as it may act as a secondary B_1 magnetic field. However, in our setup, this parasitic effect is significantly minimized by employing a frequency of 25 MHz, which is well above the Larmor frequency of 2.56 MHz. The heater signal is generated by a function generator, amplified by an RM Italy HLA150-Plus ham radio amplifier, and subsequently fed into the series connection of both ITO layers, which represents a well-matched 50-Ω load. In our current setup, the cell temperature is manually controlled by adjusting the output amplitude of the function generator. An automated PID-based temperature control

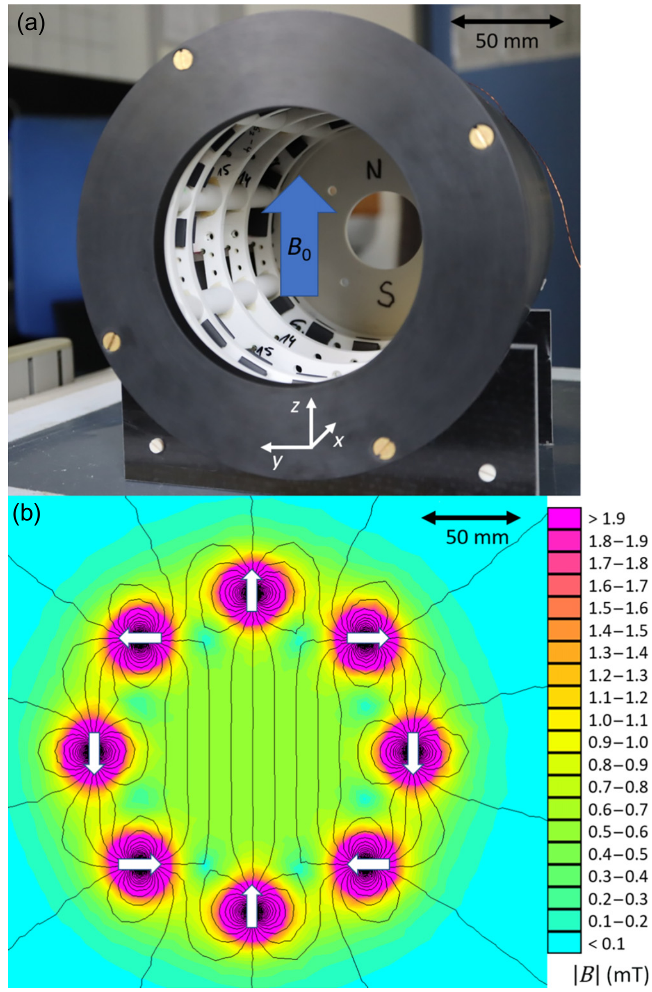

FIG. 5. (a) A photograph of the Halbach cylinder used in this work. The direction of B_0 and the coordinate system of reference are included for clarity. (b) The simulated magnetic flux density for a similar magnet configuration. The magnetic dipoles are indicated by white arrows.

loop, however, could easily be implemented in a future version. The high frequency of the heater current does result in a non-negligible capacitive coupling to nearby electrical components, such as the photodiodes. However, no adverse effects have been observed in the course of our experiments.

C. Halbach cylinder

The measurement approach imposes specific requirements on the bias-field generation to avoid compromising the performance of the OPM while allowing for the envisaged deployment for in-field use:

(1) The magnetic flux density must be in the range of 0.5 mT to 1 mT, which is substantially higher than the

typical strength of the Earth's magnetic field, while simultaneously avoiding unnecessarily large splitting caused by the NLZE.

(2) The broadening of the magnetic resonance signal due to magnetic field inhomogeneity should be negligible, meaning that it should be smaller than both the linewidth and the splitting of individual Zeeman transitions due to the NLZE. The specified maximum variations within the previously defined critical volume are $\Delta B_0 < 100$ nT, corresponding to a Larmor-frequency variation of 350 Hz. For comparison: according to Eq. (4), the splitting in $B_0 = 500\ \mu$T is about 668 Hz.

(3) Temporal variations of the bias field should be below the intrinsic noise floor of the OPM.

(4) The magnetic field outside the field-generation system should decay spatially as rapidly as possible to prevent the neighboring vector magnetometers from being affected by magnetic field gradients.

(5) The dimensions of the field-generation system should not exceed 30 cm in any spatial direction, such that a future three-axis system could fit into a transportation box that can be carried by two people.

With the above requirements, a generation of the magnetic field by coils can be ruled out according to the current state of the art. For example, with state-of-the-art current drivers as in Ref. [36], one can expect a noise floor of 714 $\mathrm{fT}/\sqrt{\mathrm{Hz}}$ when generating a bias field of 500 μT. Therefore, solid-state magnets have been used in this work. To provide the required field strength, homogeneity, and external spatial decay for the field generation, a slightly modified version of a Halbach cylinder has been designed, which is shown in Fig. 5. In theory, a Halbach cylinder is defined as a cylindrical shell the remanent magnetization of which satisfies the angular dependence

$$B_{R,r} = B_R \cos\varphi,\quad B_{R,t} = B_R \sin\varphi, \tag{8}$$

in which φ is the polar angle and B_R is the absolute value of the remanent magnetization, with the radial and tangential components $B_{R,r}$ and $B_{R,t}$, respectively [58]. The design and implementation of such a field-generation system has been carried out by Sekels GmbH [59].

The Halbach cylinder has been approximated using six ring structures. Each ring structure contains eight magnets, evenly spaced at angular intervals of $\Delta\varphi = 45^\circ$ along a circular radius of 80 mm. The orientations of the magnets correspond to Eq. (8). The ring structures have been distributed along the cylinder axis such that the volume in which $\Delta B_0 < 100$ nT applies is maximized. Including the housing, the cylinder has a diameter of 200 mm and a height of 240 mm. Simulations confirm that the stray field outside the Halbach cylinder decays sufficiently fast to allow a multichannel arrangement with a displacement of 300 mm without affecting the magnetometer performance. In order to fulfil the homogeneity specification, a larger number of magnets have been produced and characterized with regard to their magnetic moments and deviations of the angle of magnetization. Of those, 48 suitable ones have been selected. The magnets have been made of a special anisotropic Sm_2Co_{17} alloy, showing a slightly positive temperature coefficient, unlike more common materials such as neodymium or ferrite. This property helps to compensate for the thermal expansion of the frame structure (rings and spacers between the rings), which would otherwise weaken the bias field. Additionally, the frame has been constructed out of ceramic material to minimize thermal expansion. The field-generation system has been designed to have a magnetic flux density of around 730 μT, with the temperature dependence effectively neutralized slightly above room temperature.

IV. EXPERIMENTAL RESULTS

A. Field generation

In order to demonstrate the homogeneity of the bias magnetic field, the whole setup has been placed inside a three-layer magnetic shielding barrel and the sensor head has been moved in the x and y directions (for the definition of the coordinate frame, see Figs. 2 and 5) relative to the Halbach cylinder while monitoring the measured Larmor frequency. Since the sensor head fits exactly into the holding frame (not shown in Fig. 5) of the Halbach cylinder, movement in the z direction has not been possible. For the estimation of the homogeneity, it has therefore been assumed that the relative homogeneities in the y and z directions are similar for symmetry reasons. By this method, we have measured an average magnetic field magnitude of 731.8 μT at room temperature and also confirmed the specified magnetic field homogeneity.

The temperature dependence of the bias field has been determined by initially cooling or heating the Halbach cylinder to -31°C and $+62^\circ$C within a climate chamber, respectively. After each process, the Halbach cylinder has been put back into the magnetic shielding barrel within a few minutes. During the relaxation of the system back to room temperature, B_0 and the temperature have been monitored using the OPM and a PT1000 temperature sensor attached to the Halbach cylinder. The results of the cool-down and warm-up processes are shown in Fig. 6. In order to minimize the time between removal from the climate chamber and the start of the measurement, the magnetic shielding barrel has been left open on one side (without a lid). As a consequence, both measurements have been slightly affected by temporal variations of the magnetic field in the laboratory as well as by different offsets due to varying positions in the open shielding barrel. According to Fig. 6, the temperature dependence exhibits a wide plateau region, with a maximum observed

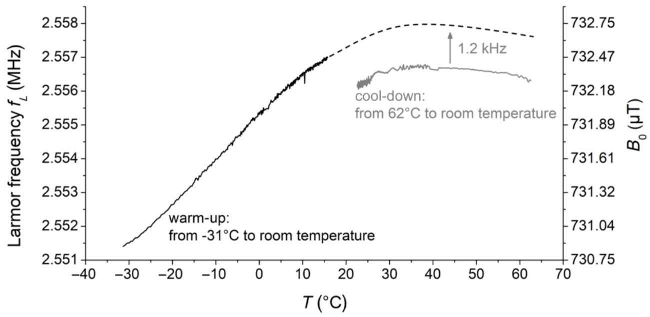

FIG. 6. The temperature dependence of the bias magnetic field B_0. The warm-up and cool-down measurements have presumably been superimposed by different magnetic offsets. A dashed line has therefore been included as a visual indicator to demonstrate that the two measurements align when shifted by 1.2 kHz relative to each other.

at approximately 40°C. We therefore assume that measurable temperature-related fluctuations in the bias field can be minimized by maintaining the Halbach cylinder at a constant temperature close to 40°C. The heating could be realized using a high-frequency current similar to that employed for cell heating, ensuring that the alternating magnetic field does not interfere with the measurements.

B. Vectorial measurement principle

The vectorial measurement principle is verified by the data shown in Fig. 7. In the figure, a magnetic field has been applied by a set of mutually orthogonal Helmholtz coils inside the shielding barrel. If the magnetic field of the coils is applied in parallel to B_0, the measured Larmor frequency exhibits a linear dependence. If, in contrast, the field is applied perpendicular to B_0, the Larmor frequency is only slightly affected by some weak quadratic perturbation. The measured data fit well to the theoretical expectations represented by Eq. (1).

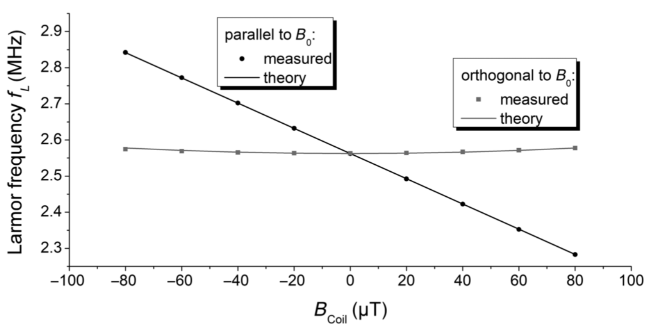

FIG. 7. The proof of the vectorial measurement principle. For a magnetic field applied parallel to the bias field B_0, the Larmor frequency increases linearly. Orthogonally applied magnetic fields, in contrast, are strongly suppressed, exhibiting only a very weak quadratic characteristic.

C. Sensitivity

The determination of the operating point with the lowest spectral magnetic noise density of the sensor can be a time-consuming process, as the operating point depends on several factors, including the wavelength and power of the laser, the amplitude of B_1, and the cell temperature. To accelerate this procedure, the operating point has therefore been initially optimized with regard to the shot-noise-limited sensitivity, which can be measured more easily, as it is not affected by external magnetic disturbances. Subsequently, the operating point of the sensor has been readjusted based on measurements of the spectral magnetic noise density, thereby attaining the operating point with optimized sensor sensitivity.

The shot-noise-limited sensitivity has been determined by sweeping the B_1 frequency through the magnetic resonance signal in open-loop mode (see Fig. 3), using

$$B_{sn} = \frac{2\pi}{\gamma_L}\frac{\sqrt{2e(I_{ph1}+I_{ph2})}}{s}, \qquad (9)$$

where $s = \partial(I_{ph1} - I_{ph2})/\partial f_{B1}$ is the slope of the differential signal at the sensor operating point and e is the elementary charge. In Eq. (9), $I_{ph1} = I_{ph2}$ can be assumed, as this corresponds to the final closed-loop operating mode.

After completing the optimization of the shot-noise-limited sensitivity, the spectral magnetic noise density of the sensor has been minimized in closed-loop operation, resulting in the noise spectrum shown in Fig. 8. In the figure, the measured spectral magnetic field noise density is below 60 $\mathrm{fT}/\sqrt{\mathrm{Hz}}$ in an interval between 100 Hz and 600 Hz and about 400 $\mathrm{fT}/\sqrt{\mathrm{Hz}}$ at 1 Hz. The operating point for this measurement has been as follows: $1/e^2$ beam diameter of 5 mm, laser power at the vapor cell approximately 9 mW for each sub-beam, $T = 125$°C, and $B_1 = 2.33$ μT (peak). As the optimal operating point has been found to be at the upper limit of the laser power, we assume that even better values could be achieved, e.g., by improving the coupling of light into the optical fiber. Between 10 Hz and 100 Hz, the spectrum is dominated by mechanical vibrations of the shielding barrel, which have already been reported in SQUID measurements [49].

Above approximately 400 Hz, the noise level increases, which we attribute to the limited intrinsic bandwidth of the OPM. However, this intrinsic open-loop bandwidth has not been explicitly measured, as only the system bandwidth in closed-loop operating mode is of interest here. The latter has been experimentally determined by applying a white-noise magnetic test signal to the magnetometer setup via a small coil. The frequency response, shown in Fig. 8, indicates a flat dependency in the range between dc and approximately 2 kHz, with a 3-dB bandwidth of approximately 5.7 kHz.

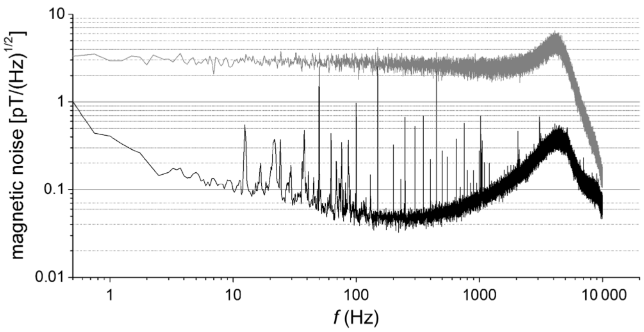

FIG. 8. The spectral magnetic noise density (black curve) of the vector magnetometer located within a three-layer shielding barrel. The OPM is exposed to a bias magnetic field of $B_0 \approx 730\ \mu\text{T}$, created by the Halbach cylinder. The bandwidth of the closed-loop operated magnetometer can be determined from the gray curve, indicating the response to a white-noise magnetic test signal.

In order to be able to interpret the experimentally obtained spectral magnetic noise density, the magnetic resonance signal has once again been measured in open-loop mode at the final operating point, resulting in the data shown in Fig. 3. From these data, the theoretical values of the fundamental and the shot-noise-limited sensitivity have been obtained according to Eqs. (5) and (9). Typically, the transverse relaxation rate Γ_2 can be obtained from the linewidth of the magnetic resonance signal. In our case, however, the linewidth is considerably broadened due to the NLZE and the strong B_1 amplitude used. Thus, an accurate determination of Γ_2 requires more effort. For our purposes, however, it is sufficient to estimate $\Gamma_2 < 10\,\text{kHz}$ from Fig. 3, resulting in $B_{sp} < 1.5\,\text{fT}/\sqrt{\text{Hz}}$ in the case of $T = 125°\text{C}$ and $V = 157\ \text{mm}^3$. The shot-noise-limited sensitivity can be calculated using the values $I_{ph1} = I_{ph2} \approx 0.83\,\text{mA}$ and $s \approx 1.3\ \mu\text{A/Hz}$ from Fig. 3, resulting in $B_{sn} \approx 5.1\ \text{fT}/\sqrt{\text{Hz}}$. These values indicate that the measured magnetic noise is at least one order of magnitude above the fundamental limits. The most obvious explanation is insufficient balancing of the two sub-beams. In this case, for example, technical noise originating from the laser is not completely compensated. An important task for future work in this field is therefore to improve the balancing of the beams and to identify and eliminate further potential noise sources.

V. SUMMARY

An approach for an OPM-based vector magnetometer has been presented, in which the vector component to be measured is traced back to a high-precision frequency measurement and therefore offers substantial potential in terms of dynamic range and sensitivity. The vector magnetometer is designed to operate within the Earth's magnetic field, with the intention of replacing SQUID-based magnetometers in several geomagnetic applications. The vectorial measurement is achieved by exposing the OPM to a strong bias field of 732 μT, which defines the sensitive axis of the vector magnetometer and ensures dead-zone-free operation with consistent sensitivity, regardless of its orientation within the Earth's magnetic field. In this bias field, a magnetic noise of $< 60\ \text{fT}/\sqrt{\text{Hz}}$ has been achieved in the interval between 100 Hz and 600 Hz, which has never been reached before with OPMs in terms of relative sensitivity. Since the estimated shot-noise-limited sensitivity of $5.1\,\text{fT}/\sqrt{\text{Hz}}$ is still about one order of magnitude below the measured magnetic noise, the latter seems to be dominated by technical noise, thus offering huge potential for further sensitivity improvements. In closed-loop operation, the vector magnetometer offers a 3-dB bandwidth of $> 5\,\text{kHz}$. This unique combination of vectorial sensitivity, very low noise, large bandwidth, and easier handling makes our approach a promising alternative to SQUID-based magnetometers for various applications.

In this work, we have chosen the LSD-Mz configuration as it naturally fits the requirement of working in a strong magnetic field with a well-defined direction. Moreover, we consider it to be best suited for dealing with the consequences arising from the nonlinear Zeeman splitting. However, the basic idea of achieving a vector magnetometer by applying a strong bias magnetic field to the OPM might also work for other operational schemes.

An excellent homogeneity and temporal stability of the bias field are essential for the performance of the vector magnetometer. For this reason, the bias field has been created by a Halbach cylinder based on precision solid-state magnets with a defined temperature coefficient. This configuration has enabled an excellent homogeneity of $\Delta B_0 < 100\,\text{nT}$ within the region of interest and a vanishing temperature dependence $B_0(T)$ without adding excess magnetic field noise.

In future work, we will analyze a further simplification of the Halbach cylinder and characterize the long-term stability of the bias magnetic field as it determines the range of application for which this type of sensor is suitable. Nevertheless, the achieved stability of the bias magnetic field up to a timescale of a few minutes seen in the laboratory is already sufficient to deploy the sensor within the intended geomagnetic application scenario of the transient electromagnetic method (TEM). Currently, we are working on portable electronics to replace the bulky laboratory equipment and allow for operation outside of the laboratory.

ACKNOWLEDGMENTS

We gratefully acknowledge financial support from the Federal Ministry of Education and Research (BMBF) of Germany under the project Optisch gepumpte Quantenmagnetometer für Transiente Elektromagnetik (Grant No. 13N15436).

DATA AVAILABILITY

The data that support the findings of this article are openly available [60].

[1] M. Hämäläinen, R. Hari, R. J. Ilmoniemi, J. Knuutila, and O. V. Lounasmaa, Magnetoencephalography—theory, instrumentation, and applications to noninvasive studies of the working human brain, Rev. Mod. Phys. **65**, 413 (1993).

[2] H. Koch, Recent advances in magnetocardiography, J. Electrocardiol. **37**, 117 (2004).

[3] R. Hohmann, H.-J. Krause, H. Soltner, H. Zhang, C. Copetti, H. Bousack, A. Braginski, and M. Faley, HTS SQUID system with Joule-Thomson cryocooler for eddy current nondestructive evaluation of aircraft structures, IEEE Trans. Appl. Supercond. **7**, 2860 (1997).

[4] P. A. Koss, A. R. Durmaz, A. Blug, G. Laskin, O. S. Pawar, K. Thiemann, A. Bertz, T. Straub, and C. Elsässer, Optically pumped magnetometer measuring fatigue-induced damage in steel, Appl. Sci. **12**, 1329 (2022).

[5] P. Sharma, Magnetic method applied to mineral exploration, Ore Geol. Rev. **2**, 323 (1987).

[6] S. Billings, Discrimination and classification of buried unexploded ordnance using magnetometry, IEEE Trans. Geosci. Remote Sens. **42**, 1241 (2004).

[7] M. Munschy, D. Boulanger, P. Ulrich, and M. Bouiflane, Magnetic mapping for the detection and characterization of UXO: Use of multi-sensor fluxgate 3-axis magnetometers and methods of interpretation, J. Appl. Geophys. **61**, 168 (2007), state-of-the-Art UXO Detection and Characterization.

[8] A. Clark, *Seeing Beneath the Soil: Prospecting Methods in Archaeology* (Batsford, London, 1990).

[9] J. W. Fassbinder, Seeing beneath the farmland, steppe and desert soil: Magnetic prospecting and soil magnetism, J. Archaeol. Sci. **56**, 85 (2015), scoping the Future of Archaeological Science: Papers in Honour of Richard Klein.

[10] M. Schmelz, V. Zakosarenko, A. Chwala, T. Schönau, R. Stolz, S. Anders, S. Linzen, and H.-G. Meyer, Thin-film-based ultralow noise SQUID magnetometer, IEEE Trans. Appl. Supercond. **26**, 1 (2016).

[11] J. C. Allred, R. N. Lyman, T. W. Kornack, and M. V. Romalis, High-sensitivity atomic magnetometer unaffected by spin-exchange relaxation, Phys. Rev. Lett. **89**, 130801 (2002).

[12] I. K. Kominis, T. W. Kornack, J. C. Allred, and M. V. Romalis, A subfemtotesla multichannel atomic magnetometer, Nature **422**, 596 (2003).

[13] S. J. Seltzer and M. V. Romalis, Unshielded three-axis vector operation of a spin-exchange-relaxation-free atomic magnetometer, Appl. Phys. Lett. **85**, 4804 (2004).

[14] H. B. Dang, A. C. Maloof, and M. V. Romalis, Ultrahigh sensitivity magnetic field and magnetization measurements with an atomic magnetometer, Appl. Phys. Lett. **97**, 151110 (2010).

[15] S. Appelt, A. Ben-Amar Baranga, A. R. Young, and W. Happer, Light narrowing of rubidium magnetic-resonance lines in high-pressure optical-pumping cells, Phys. Rev. A **59**, 2078 (1999).

[16] S. J. Smullin, I. M. Savukov, G. Vasilakis, R. K. Ghosh, and M. V. Romalis, Low-noise high-density alkali-metal scalar magnetometer, Phys. Rev. A **80**, 033420 (2009).

[17] D. Sheng, S. Li, N. Dural, and M. V. Romalis, Subfemtotesla scalar atomic magnetometry using multipass cells, Phys. Rev. Lett. **110**, 160802 (2013).

[18] M. Limes, E. Foley, T. Kornack, S. Caliga, S. McBride, A. Braun, W. Lee, V. Lucivero, and M. Romalis, Portable magnetometry for detection of biomagnetism in ambient environments, Phys. Rev. Appl. **14**, 011002 (2020).

[19] G. Oelsner, R. IJsselsteijn, T. Scholtes, A. Krüger, V. Schultze, G. Seyffert, G. Werner, M. Jäger, A. Chwala, and R. Stolz, Integrated optically pumped magnetometer for measurements within Earth's magnetic field, Phys. Rev. Appl. **17**, 024034 (2022).

[20] W. Fourcault, R. Romain, G. L. Gal, F. Bertrand, V. Josselin, M. L. Prado, E. Labyt, and A. Palacios-Laloy, Helium-4 magnetometers for room-temperature biomedical imaging: Toward collective operation and photon-noise limited sensitivity, Opt. Express **29**, 14467 (2021).

[21] M. N. Nabighian, ed., in *Electromagnetic Methods in Applied Geophysics: Volume 2, Application, Parts A and B* (Society of Exploration Geophysicists, Tulsa, Oklahoma, 1991), p. 427.

[22] A. J. Fairweather and M. J. Usher, A vector rubidium magnetometer, J. Phys. E: Sci. Instrum. **5**, 986 (1972).

[23] W.-M. Sun, Q. Huang, Z.-J. Huang, P.-W. Wang, and J.-H. Zhang, All-optical vector cesium magnetometer, Chin. Phys. Lett. **34**, 058501 (2017).

[24] S. Afach *et al.*, Highly stable atomic vector magnetometer based on free spin precession, Opt. Express **23**, 22108 (2015).

[25] H. Lee, M. Fleischhauer, and M. O. Scully, Sensitive detection of magnetic fields including their orientation with a magnetometer based on atomic phase coherence, Phys. Rev. A **58**, 2587 (1998).

[26] K. Cox, V. I. Yudin, A. V. Taichenachev, I. Novikova, and E. E. Mikhailov, Measurements of the magnetic field vector using multiple electromagnetically induced transparency resonances in Rb vapor, Phys. Rev. A **83**, 015801 (2011).

[27] S. Pustelny, W. Gawlik, S. M. Rochester, D. F. J. Kimball, V. V. Yashchuk, and D. Budker, Nonlinear magneto-optical rotation with modulated light in tilted magnetic fields, Phys. Rev. A **74**, 063420 (2006).

[28] V. Acosta, M. P. Ledbetter, S. M. Rochester, D. Budker, D. F. Jackson Kimball, D. C. Hovde, W. Gawlik, S. Pustelny, J. Zachorowski, and V. V. Yashchuk, Nonlinear magneto-optical rotation with frequency-modulated light in the geophysical field range, Phys. Rev. A **73**, 053404 (2006).

[29] L. Lenci, A. Auyuanet, S. Barreiro, P. Valente, A. Lezama, and H. Failache, Vectorial atomic magnetometer based on coherent transients of laser absorption in Rb vapor, Phys. Rev. A **89**, 043836 (2014).

[30] E. B. Alexandrov, M. V. Balabas, V. N. Kulyasov, A. E. Ivanov, A. S. Pazgalev, J. L. Rasson, A. K. Vershovski, and N. N. Yakobson, Three-component variometer based on a scalar potassium sensor, Meas. Sci. Technol. **15**, 918 (2004).

[31] A. K. Vershovskii, M. V. Balabas, A. E. Ivanov, V. N. Kulyasov, A. S. Pazgalev, and E. B. Aleksandrov, Fast three-component magnetometer-variometer based on a cesium sensor, Techn. Phys. **51**, 112 (2006).

[32] J.-M. Leger, F. Bertrand, T. Jager, M. Le Prado, I. Fratter, and J.-C. Lalaurie, Swarm absolute scalar and vector magnetometer based on helium 4 optical pumping, Proc. Chem. **1**, 634 (2009), proceedings of the Eurosensors XXIII conference.

[33] G. Hulot, P. Vigneron, J.-M. Léger, I. Fratter, N. Olsen, T. Jager, F. Bertrand, L. Brocco, O. Sirol, X. Lalanne, A. Boness, and V. Cattin, Swarm's absolute magnetometer experimental vector mode, an innovative capability for space magnetometry, Geophys. Res. Lett. **42**, 1352 (2015).

[34] G. Zhang, H. Zeng, R. Guo, Q. Zhang, W. Yu, and Q. Lin, Light-narrowed parametric resonance magnetometer with the fundamental sensitivity beyond the spin-exchange limit, Opt. Lett. **48**, 4793 (2023).

[35] B. Patton, E. Zhivun, D. C. Hovde, and D. Budker, All-optical vector atomic magnetometer, Phys. Rev. Lett. **113**, 013001 (2014).

[36] F. Bertrand, T. Jager, A. Boness, W. Fourcault, G. Le Gal, A. Palacios-Laloy, J. Paulet, and J. M. Léger, A ^{4}He vector zero-field optically pumped magnetometer operated in the Earth-field, Rev. Sci. Instrum. **92**, 105005 (2021).

[37] T. Schönau, T. Scholtes, R. Stolz, and G. Oelsner, Vektorielles, optisch gepumptes Magnetometer mit einer hohen Empfindlichkeit (2024), DE102024101952.2.

[38] G. Breit and I. I. Rabi, Measurement of nuclear spin, Phys. Rev. **38**, 2082 (1931).

[39] G. K. Woodgate, *Elementary Atomic Structure* (Oxford University Press, Oxford, 1980).

[40] P. D. D. Schwindt, L. Hollberg, and J. Kitching, Self-oscillating rubidium magnetometer using nonlinear magneto-optical rotation, Rev. Sci. Instrum. **76**, 126103 (2005).

[41] J. Hinkel, Master's thesis, Optically pumped magnetometers for use in high background fields, Technical University of Applied Sciences Wildau & University of Rome Tor Vergata.

[42] G. Bao, D. Kanta, D. Antypas, S. Rochester, K. Jensen, W. Zhang, A. Wickenbrock, and D. Budker, All-optical spin locking in alkali-metal-vapor magnetometers, Phys. Rev. A **105**, 043109 (2022).

[43] V. Schultze, B. Schillig, R. IJsselsteijn, T. Scholtes, S. Woetzel, and R. Stolz, An optically pumped magnetometer working in the light-shift dispersed Mz mode, Sensors **17**, 561 (2017).

[44] G. Oelsner, V. Schultze, R. IJsselsteijn, and R. Stolz, Performance analysis of an optically pumped magnetometer in Earth's magnetic field, EPJ Quantum Technol. **6**, 6 (2019).

[45] T. Scholtes, V. Schultze, R. IJsselsteijn, S. Woetzel, and H.-G. Meyer, Light-narrowed optically pumped M_x magnetometer with a miniaturized Cs cell, Phys. Rev. A **84**, 043416 (2011).

[46] T. Scholtes, S. Pustelny, S. Fritzsche, V. Schultze, R. Stolz, and H.-G. Meyer, Suppression of spin-exchange relaxation in tilted magnetic fields within the geophysical range, Phys. Rev. A **94**, 013403 (2016).

[47] D. Budker and D. F. Jackson Kimball, eds. *Optical Magnetometry* (Cambridge University Press, Cambridge, 2013).

[48] V. P. I. C. B. Alcock and M. K. Horrigan, Vapour pressure equations for the metallic elements: 298–2500K, Can. Metall. Q. **23**, 309 (1984).

[49] V. Schultze, R. IJsselsteijn, and H.-G. Meyer, Noise reduction in optically pumped magnetometer assemblies, Appl. Phys. B **100**, 717 (2010).

[50] W. E. Bell and A. L. Bloom, Optical detection of magnetic resonance in alkali metal vapor, Phys. Rev. **107**, 1559 (1957).

[51] W. E. Bell and A. L. Bloom, Optically driven spin precession, Phys. Rev. Lett. **6**, 280 (1961).

[52] Z. D. Grujić, P. A. Koss, G. Bison, and A. Weis, A sensitive and accurate atomic magnetometer based on free spin precession, Eur. Phys. J. D **69**, 135 (2015).

[53] Z. D. Grujić, M. Ćurĉić, A. Kocić, A. Weis, and T. Scholtes, Phase projection errors in rf-driven optically pumped magnetometers, arXiv:2409.20446.

[54] B. S. Mathur, H. Tang, and W. Happer, Light shifts in the alkali atoms, Phys. Rev. **171**, 11 (1968).

[55] G. Oelsner, V. Schultze, R. IJsselsteijn, F. Wittkämper, and R. Stolz, Sources of heading errors in optically pumped magnetometers operated in the Earth's magnetic field, Phys. Rev. A **99**, 013420 (2019).

[56] S. Woetzel, V. Schultze, R. IJsselsteijn, T. Schulz, S. Anders, R. Stolz, and H.-G. Meyer, Microfabricated atomic vapor cell arrays for magnetic field measurements, Rev. Sci. Instrum. **82**, 033111 (2011).

[57] T. G. Walker and W. Happer, Spin-exchange optical pumping of noble-gas nuclei, Rev. Mod. Phys. **69**, 629 (1997).

[58] R. Bjørk, The ideal dimensions of a Halbach cylinder of finite length, J. Appl. Phys. **109**, 013915 (2011).

[59] Sekels GmbH, Dieselstrasse 6, 61239 Ober-Mörlen, Germany (https://sekels.de/).

[60] T. Schönau, Zenodo, Version V2, Dez. 19, 2024, http://doi.org/10.5281/zenodo.14709938.